Nano Research 2018, 11(5): 2756–2770
https://doi.org/10.1007/s12274-017-1906-7
Research Article
ISSN 1998-0124
CN 11-5974/O4

Targeted and imaging-guided *in vivo* photodynamic therapy for tumors using dual-function, aggregation-induced emission nanoparticles

Xianhe Sun[1,§], Abudureheman Zebibula[2,§], Xiaobiao Dong[3], Gonghui Li[2] (✉), Guanxin Zhang[3] (✉), Deqing Zhang[3], Jun Qian[1], and Sailing He[1,4] (✉)

[1] *State Key Laboratory of Modern Optical Instrumentations, Centre for Optical and Electromagnetic Research, Zhejiang University, Hangzhou 310058, China*
[2] *Department of Urology, Sir Run Run Shaw Hospital, College of Medicine, Zhejiang University, Hangzhou 310016, China*
[3] *Beijing National Laboratory for Molecular Sciences, CAS Key Laboratories of Organic Solids and Analytical Chemistry for Living Biosystems, Institute of Chemistry, Chinese Academy of Sciences, Beijing 100190, China*
[4] *School of Electrical Engineering, Royal Institute of Technology, OSQULDAS VÄG 6, Stockholm SE-100 44, Sweden*
[§] *Xianhe Sun and Abudureheman Zebibula contributed equally to this work.*

Received: 5 June 2017
Revised: 1 November 2017
Accepted: 3 November 2017

KEYWORDS
aggregation-induced emission,
targeted therapy,
imaging-guided therapy,
photodynamic therapy,
tumor

ABSTRACT

Imaging-guided photodynamic therapy (PDT) has been regarded as a promising strategy for precise cancer treatment. Because of their excellent modifiability and drug-loading capacity, nanoparticles have played an important role in PDT. Nonetheless, when traditional photosensitizers are made into nanoparticles, both their fluorescence and reactive oxygen species generation efficacy decrease due to a phenomenon known as aggregation-caused quenching. Fortunately, in recent years, several kinds of organic dyes with "abnormal" properties (termed aggregation-induced emission, AIE) were developed. With enhanced fluorescence emission in the nanoaggregation state, the traditional obstacles mentioned above may be overcome by AIE luminogens. Herein, we provide a better combination of photosensitizers and nanoparticles, namely, dual-function AIE nanoparticles capable of producing reactive oxygen species, to implement targeted and imaging-guided *in vivo* PDT. Good contrast of *in vivo* imaging and obvious therapeutic efficacy were observed at a low dose of AIE nanoparticles and low irradiance of light, thus resulting in negligible side effects. Our work shows that AIE nanoparticles may play a promising role in imaging-guided clinical PDT for cancer in the near future.

Address correspondence to Sailing He, sailing@kth.se; Gonghui Li, Lgh_002@163.com; Guanxin Zhang, gxzhang@iccas.ac.cn

1 Introduction

Cancer has increasingly become a primary threat to human health, and more effective treatment methods are urgently needed [1–5]. Conventional cancer treatment methods, including surgery, chemotherapy, and radiotherapy, lack accuracy and have significant adverse effects [6–10]. Therefore, much attention has been given to the development of novel treatment modalities [11–15]. Imaging-guided photodynamic therapy (PDT) has been developed and shown to be an effective, precise, and noninvasive medical technique for cancer therapy [16–20]. The photodynamic effect consists of three elements: A photosensitizer (PS), light of a suitable wavelength, and oxygen. Briefly, the energy of light can be utilized to transform nontoxic triplet oxygen into toxic reactive oxygen species (ROS). Because the process occurs only when both the PS and light of a particular wavelength are present together, this method can provide good selectivity for a treatment region [21–23]. Meanwhile, most PSs show fluorescence emission [23, 24], and with the guidance of fluorescent images, PDT can be a rather precise treatment modality.

Along with the development of nanotechnology, various series of colloidal nanoparticles have become powerful tools in PDT [25–28]. Because the nanometer scale provides a high surface-to-volume ratio, nanoparticles can ensure high drug-loading capacity as well as effective surface chemical modification. High drug-loading capacity leads to fewer adverse effects, while surface chemical modification allows for customized designs, which can greatly improve the specific properties of drugs, such as hydrophilicity [29] and targeting ability [30–33]. In addition, the "enhanced permeability and retention" effect, a characteristic of tumor tissue, enables nanoparticles to pass through loose vascular tissue and accumulate in the tumor tissue, providing a passive way of targeted drug delivery [34, 35]. For most PSs, however, especially widely used porphyrin derivatives, π–π stacking occurs when they are made into nanoparticles, owing to their hydrophobic and rigid planar structures. This drawback can result in aggregation-induced quenching of fluorescence [36] and an obvious reduction in ROS production [37]; these phenomena limit the performance of optical imaging and the efficacy of imaging-guided PDT. Fortunately, some inorganic nanoparticles as PSs for PDT have been reported [38, 39]. Nevertheless, the development of new effective organic nanosensitizers is still necessary from the standpoint of biocompatibility and biosafety.

Aggregation-induced emission (AIE), an "abnormal" effect discovered in 2001, may provide a solution to the dilemma mentioned above [40–42]. Organic propeller-shaped AIE luminogens (AIEgens), such as tetraphenylethene (TPE) and silole derivatives, are nonemissive or weakly emissive in benign solvents (usually organic solvents) but become much brighter when forming aggregates in poor solvents (e.g., water) [43]. Fabricating AIEgens into nanoparticles takes advantage of their nature, thus changing the obstacles to an opportunity and further benefiting PDT for tumors. In the field of PDT, AIEgens have been reported to be combined with popular PSs, such as PpIX, acting as a sensing probe [44] or an enhancer for ROS production [45, 46]. AIE nanoparticles have also been used only as a PS (not a fluorophore) to implement *in vivo* PDT via intratumoral injection [47]. In these studies, AIEgens have served as a sensing probe, an energy donor, or just a PS. The procedures have been complex, and the potential of AIE materials has been utilized only partially. In fact, AIE nanoparticles can be a good PS as well as a fluorescent label. Recently, some AIEgens with the ability to produce ROS themselves have been synthesized and tested for *in vitro* one-photon PDT [48, 49] and two-photon PDT for cancer cells and blood vessels [50]. Very recently, one study showed attempts to achieve imaging-guided and targeted *in vivo* PDT by means of AIE nanoparticles alone in a dose of 30 $mg \cdot kg^{-1}$ [51]. By contrast, in the present independent work, we achieved targeted *in vivo* imaging and a similar antitumor efficacy (tumor inhibition of 60.4%) at a dose as low as 10 $mg \cdot kg^{-1}$, which may cause less biological toxicity and side effects.

Herein, we fabricated dual-function AIE nanoparticles based on a widely used AIEgen, 2-((4-(2,2-bis(4-methoxyphenyl)-1-phenylvinyl)phenyl)(phenyl)methylene) malononitrile (TPE-red), which can be easily synthesized and has an outstanding ability to produce ROS [52, 53]. To enhance tumor targeting, promote

endocytosis, and ensure a therapeutic effect, we modified the nanoparticles with a customized peptide, cyclic (Arg-Gly-Asp-d-Phe-Cys) (c(RGDfc)), a group commonly used to target overexpressed integrin $\alpha_v\beta_3$ in most cancer cells [54]. As illustrated in Scheme 1(b), the polyethylene glycol (PEG) and RGD-modified TPE-red (TPE-red-PEG-RGD) nanoparticles were intravenously injected into tumor-bearing mice. These nanoparticles can target the tumor tissues in both passive and active ways, get internalized by cancer cells, and finally produce ROS when subjected to suitable irradiation. Compared with common PSs, the AIE nanoparticles we fabricated are free of the aggregation-caused quenching effect. Taking advantage of bright fluorescence emission, high targeting efficacy, and outstanding capacity for ROS production, we could achieve targeted imaging of tumor regions and high antitumor efficacy at a rather low dose, which may cause fewer adverse effects. Furthermore, TPE-red-PEG-RGD nanoparticles are rather simple and easy to make as compared with composite structures; this approach can facilitate further research and mass production.

2 Experimental

2.1 Materials

All reagents and solvents were purchased from commercial sources and used without further purification. 1,2-Distearoyl-sn-glycero-3-phosphoethanolamine-N-[maleimide (polyethylene glycol)-2000] (DSPE-PEG_{2000}-Mal) was purchased from JenKem Technology Co., Ltd. TPE-red was synthesized according to our previous report [52]. c(RGDfc) was custom-made by GL Biochem, Ltd. (Shanghai). 9,10-Anthracenediylbis (methylene) dimalonic acid (ABDA) and 3-(4,5-dimethylthiazol-2-yl)-2,5-diphenyltetrazolium bromide (MTT) were acquired from Sigma-Aldrich (Shanghai, China). Minimum essential medium (MEM), Dulbecco's modified Eagle's medium (DMEM), the RPMI 1640 medium, fetal bovine serum (FBS), and a trypsin-EDTA solution were purchased from Gibco. Tetrahydrofuran (THF), dimethyl sulfoxide (DMSO), hydrochloric acid, and PBS (1×) were obtained from the Chemical Reagent Department of Zhejiang University. Deionized (DI) water, with resistivity of 18.2 MΩ·cm, was used in all the experiments.

2.2 Preparation of TPE-red-PEG-RGD nanoparticles

First, TPE-red-PEG nanoparticles were fabricated by a modified nanoprecipitation method [55]. Briefly, 0.335 mL of TPE-red solutions in THF (1 mg·mL^{-1}) and 0.5 mL of DSPE-PEG2000-Mal solutions in THF (1.2 mg·mL^{-1}) were mixed gently in a flask (25 mL). The mixture was then dried in vacuum in a rotary evaporator at room temperature. When the THF was completely removed, 5 mL of PBS (1×) was added into the flask, and the solution was sonicated for several

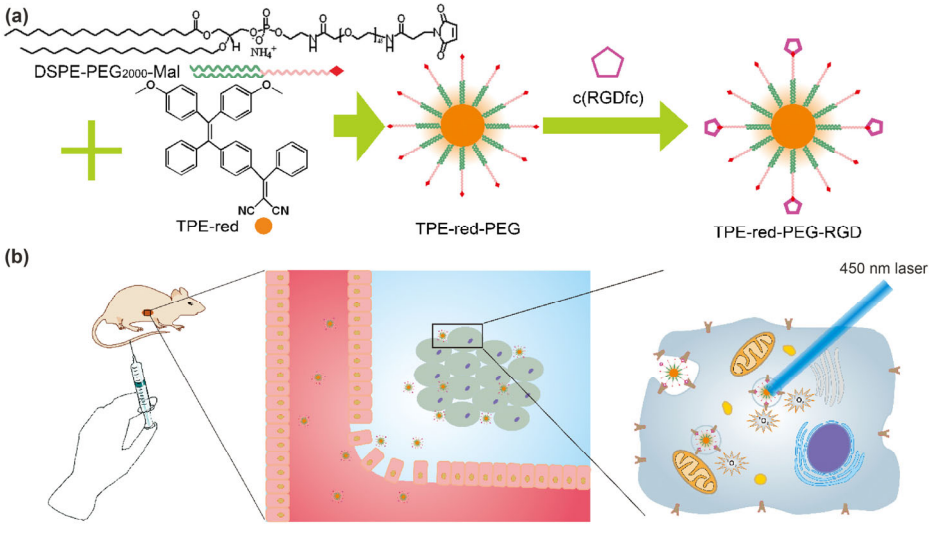

Scheme 1 Schematic illustration of (a) the fabrication procedure of TPE-red-PEG-RGD nanoparticles and (b) the process of targeted and image-guided *in vivo* PDT for cancer, via intravenous injection.

minutes to form an optically clear suspension.

To synthesize TPE-red-PEG-RGD nanoparticles, the pH value of the as-prepared TPE-red-PEG nanoparticle solution was adjusted to 5.0–7.0, and then 2 mg of a c(RGDfc) powder was added in a nitrogen atmosphere to start the reaction. The mixture was stirred overnight to ensure a complete reaction, and the reaction product was washed with DI water via dialysis for 2 days. After that, the obtained solution was filtered through a 0.22-μm microporous membrane, concentrated by evaporation of water, and finally stored at 4 ℃ for further use.

2.3 Measurement of the efficacy of c(RGDfc) conjugation to TPE-red-PEG

Because the conjugation is based on a click chemistry reaction between thiol and maleimide, the conjugation efficacy of c(RGDfc) was calculated from the concentration of thiol. We detected the concentration of thiol using Ellman's reagent [56].

Briefly, Reaction Buffer was prepared as 0.1 M sodium phosphate containing 1 mM EDTA, and the pH value was adjusted to 8.0. An Ellman's reagent solution was prepared by dissolving 4 mg of Ellman's reagent in 1 mL of Reaction Buffer. Next, 250 μL of a sample, 50 μL of the Ellman's reagent solution, and 2.5 mL of Reaction Buffer were mixed to react at room temperature for 15 min. Then, absorption of the resultant solution at 412 nm was measured on a spectrophotometer. The concentration of sulfhydryl in the sample was calculated according to the molar extinction coefficient of TNB (14,150 $M^{-1}\cdot cm^{-1}$).

2.4 Characterization

Transmission electron microscopy (TEM) images were captured under a JEOL JEM-1200 transmission electron microscope operating at 80 kV in bright-field mode. The absorption spectra of the nanoparticles were acquired on a Shimadzu 2550 UV-vis scanning spectrophotometer. The hydrodynamic size distribution of the nanoparticles was measured on a Malvern Zetasizer Nano ZS-90.

2.5 Recording of fluorescence spectra

As illustrated in Fig. S1 in the Electronic Supplementary Material (ESM), a lab-built fluorescence detection system was used to record the one-photon and two-photon-excited fluorescence spectra. Briefly, samples in a cuvette were excited by a focused laser beam, and the fluorescence signals were collected laterally by an objective lens (20×, NA = 0.75) and recorded by the spectrometer. In the case of one-photon-excited fluorescence, a 450-nm semiconductor laser was employed as the excitation source, and the spectra were recorded on a spectrometer, PG 2000, Ideaoptics. In the case of two-photon-excited fluorescence, a 1,040-nm fs laser (from an amplified output of a large-mode-area ytterbium-doped photonic crystal fiber (PCF) oscillator (1,040 nm, 150 fs, 50 MHz)) [57] served as the excitation source, and the spectra were acquired on the spectrometer QE 6500, Ocean Optics.

2.6 Power dependence of two-photon-excited fluorescence

A series of spectra according to different excitation power levels were obtained by the method described above. Based on the spectra, the intensity of fluorescence was calculated as the integral of spectrum envelopes from 500 to 670 nm. Then, we built a scatter plot of fluorescence intensity and the square of incident power, and fitted the points linearly to verify the linear relation between them.

2.7 Measurement of two-photon absorption cross-section (TPACS)

We measured TPACS by a comparison method. Specifically, the TPACS of TPE-red-PEG-RGD nanoparticles was compared with that of a common dye, rhodamine B (RhB) [58]. Using the system shown in Fig. S1 in the ESM, we acquired the spectra of RhB and TPE-red-PEG-RGD nanoparticles under the same conditions of 1,040 nm laser excitation. The fluorescence intensity was determined by integrating the spectral envelope. The TPACS of TPE-red-RED-RGD nanoparticles was calculated according to Eq. (1) [59]

$$\frac{\delta_1}{\delta_0}=\frac{F_1\eta_0 c_0 n_0}{F_0\eta_1 c_1 n_1} \quad (1)$$

where δ is the TPACS, F is the two-photon-excited

fluorescence intensity, η is the fluorescence quantum yield (QY), c is molar concentration, n is the refractive index of the solvent, and subscripts 0 and 1 represent the reference (RhB in methanol) and the sample (TPE-red-PEG-RGD nanoparticles in PBS), respectively.

Among these parameters, only the QY of TPE-red-PEG-RGD nanoparticles is still unknown, and we measured it also by the comparison with RhB.

By means of the system shown in Fig. S1 in the ESM, we determined the spectra of RhB and TPE-red-PEG-RGD nanoparticles under the same conditions of one-photon excitation. The fluorescence intensity was determined by integrating the spectral envelope. The QY of TPE-red-PEG-RGD nanoparticles was calculated according to Eq. (2) [60]

$$\frac{\eta_1}{\eta_0} = \frac{A_0}{A_1} \cdot \frac{F_1}{F_0} \cdot \frac{I_0}{I_1} \cdot \frac{n_1^2}{n_0^2} \quad (2)$$

where η is the fluorescence QY, A is absorption, F is the one-photon fluorescence intensity, I is the intensity of the laser, n is the refractive index of the solvent, and subscripts 0 and 1 represent the reference (RhB in methanol) and the sample (TPE-red-PEG-RGD nanoparticles in PBS), respectively.

2.8 ROS detection *ex vivo*

ABDA was used to evaluate the production of ROS by TPE-red-PEG-RGD nanoparticles. A 200-μL sample of an ABDA solution in DMSO was added into 2 mL of an aqueous dispersion of TPE-red-PEG-RGD nanoparticles (50 μg·mL^{-1}). The solution was mixed evenly and irradiated with a 450 nm semiconductor laser. The absorption spectra of the mixture were recorded after laser irradiation at various time points, and the decrease in absorption at 378 nm served as the indicator of ROS. The same mixture without laser irradiation served as a control.

2.9 *In vitro* experiments

2.9.1 *Cell culture*

UMUC3 cells (human bladder cancer cell line), HeLa cells (human cervical cancer cell line), and A549 cells (human pulmonary carcinoma cell line) were obtained from the Cell Culture Center of the Institute of Basic Medical Sciences, Chinese Academy of Medical Sciences (Shanghai, China). UMUC3 cells, HeLa cells, and A549 cells were grown in MEM, DMEM, and RPMI 1640, respectively. The culture media were all supplemented with 10% of FBS, 1% of a penicillin solution, and 1% of an amphotericin B solution. The incubator was kept at 37 ℃ and 5% CO_2.

2.9.2 *In vitro cell imaging*

We applied the nanoparticle-treated cells to verify the ability of the nanoparticles to get absorbed by the cells. One day before the treatment, UMUC3 cells, HeLa cells, and A549 cells were seeded in 35-mm cultivation dishes at confluence of 50% to 60%. During the treatment, the cells were incubated with the appropriate concentration of TPE-red-PEG-RGD nanoparticles for ~ 2 h. Cells treated with PBS served as a control. After that, the cells were all washed thrice with PBS and directly imaged using a microscope.

Two-photon-excited fluorescence is considered an outstanding imaging method owing to the greater penetration depth, a minimal tissue autofluorescence background, and reduced photodamage to tissues [61].

In our experiment, two-photon-excited fluorescence was utilized for *in vitro* cell imaging. As illustrated in Fig. S4 in the ESM, the imaging system consisted of an upright scanning microscope (Olympus, BX61+FV1200) equipped with a 1,040 nm fs laser (from an amplified output of a large-mode-area ytterbium-doped PCF oscillator (1,040 nm, 150 fs, 50 MHz)). The 1,040 nm fs laser beam was guided into the upright scanning microscope and focused onto the cell samples by a 60×/1.00 (Olympus) or a 20×/0.75 (Olympus) water-immersed objective lens to induce two-photon excitation. The signals with an integration period of 10 μs per pixel were epi-collected by the same objective lens. After passing through a 590-nm long-pass filter, a 570 nm dichroic mirror, and a 570–625 nm bandpass filter, the fluorescence signals were finally detected by a photomultiplier tube in nondescanned detection mode.

One-photon-excited fluorescence images were obtained by means of a fluorescence microscope equipped with a 40× objective lens. The imaged UMUC3 cells were first incubated with TPE-red-PEG-RGD nanoparticles, and then the cell nuclei were

stained with Hoechst 33258 after 2 h of incubation. The fluorescence (between 570 and 640 nm) of TPE-red-PEG-RGD nanoparticles was collected upon excitation at 450 nm, and the blue fluorescence (between 435 and 485 nm) of Hoechst 33258 was collected after excitation at 350 nm.

2.9.3 *MTT assay*

In vitro cytotoxicity was measured by MTT assays of UMUC3 cells. The cells were seeded in a 96-well culture plate at 5×10^3 per well and cultivated at 37 °C and 5% CO_2 for 24 h. Next, 200 μL of fresh MEM containing different concentrations of TPE-red-PEG-RGD nanoparticles (0, 5, 10, 20, or 50 $\mu g \cdot mL^{-1}$) was added into the wells. The cells were then incubated for 48 h at 37 °C and 5% CO_2. For each concentration, half of the cells were irradiated with 450 nm light (40 mW, 200 $mW \cdot cm^{-2}$) after 2 h incubation, while the other half was kept in the dark. After that, MTT (20 μL per well, 5 $mg \cdot mL^{-1}$) was added into each well, and the plate was incubated for additional 4 h at 37 °C and 5% CO_2. The medium was then replaced with 200 μL of DMSO per well, and OD_{570} was monitored on an enzyme-linked immunosorbent assay (ELISA) microplate reader.

To study the viability of UMUC3 cells irradiated for different periods after treatment with the same concentration of nanoparticles, we irradiated the UMUC3 cells for different time periods (2, 4, 6, or 8 min) after incubating them with 20 $\mu g \cdot mL^{-1}$ TPE-red-PEG-RGD nanoparticles for 2 h. After that, the cell viability was measured after incubation for 48 h by the method introduced above.

2.10 *In vivo* experiments

All *in vivo* experiments were conducted in compliance with Zhejiang University Animal Study Committee's requirements for the care and use of laboratory animals in research. The animal housing area (located at the Animal Experimentation Center of Zhejiang University) was maintained at 24 °C in a 12 h light/dark cycle, and the animals were provided with water and standard laboratory chow.

2.10.1 *Tumor xenograft models*

A UMUC3 tumor model was established by the subcutaneous injection of UMUC3 cells (5×10^6 $cells \cdot mL^{-1}$) into selected sites on male nude mice (5 weeks old, purchased from Slaccas Co., Ltd., Shanghai, Chinese Academy of Sciences). To determine tumor size, the major length and width of the tumors were measured using a Vernier caliper. The tumor volume was calculated as length × $width^2$ × 0.5.

2.10.2 *In vivo fluorescence imaging*

This imaging was performed by means of Iris Spectrum (Perkin Elmer). When tumor volume reached ~ 50 mm^3, 200 μL of a dispersion of TPE-red-PEG-RGD nanoparticles in 1× PBS (1 $mg \cdot mL^{-1}$) was intravenously injected into the mice. The fluorescence imaging was carried out at 24, 48, and 72 h post-injection. Spectra of fluorescence signals and autofluorescence signals were collected from the tail in the experimental group and from the back in the control group, respectively. Afterwards, regions of interest (ROIs) were circled around a tumor, and the fluorescence intensities were analyzed in Living Image® Software 4.4. The changing tendency of the amount of TPE-red-PEG-RGD nanoparticles accumulated at a tumor site was plotted as a time course line chart.

2.10.3 *Ex vivo fluorescence imaging*

Six tumor-bearing mice were randomly distributed into two groups. Mice in the experimental group were intravenously injected with TPE-red-PEG-RGD nanoparticles (10 $mg \cdot kg^{-1}$), while mice in the control group were injected with PBS (1×). The fluorescence imaging of a tumor and major organs was performed at 24, 48, and 72 h post-injection. ROIs were circled around the tumor and major organs, and the fluorescence intensities were analyzed in Living Image® Software 4.4.

2.10.4 *In vivo PDT*

When tumor volume reached ~ 50 mm^3, 16 tumor-bearing mice were randomly subdivided into four groups. The treatment scheme was as follows: (1) PBS, without irradiation; (2) PBS, with irradiation; (3) TPE-red-PEG-RGD nanoparticles (10 $mg \cdot kg^{-1}$), without irradiation; and (4) TPE-red-PEG-RGD nanoparticles (10 $mg \cdot kg^{-1}$), with irradiation. The photoirradiation was applied at 1, 2, and 3 days after the injection

(450 nm, 200 mW·cm^{-2}, for 20 min). The tumor sizes and body weights were inspected every other day for the first 4 days and every day afterwards. The tumor growth inhibition rate was calculated using the following formula: ([1 – average volume of PDT-treated tumors] ÷ average volume of tumors in control group) × 100%.

The observation lasted for 14 days. After that, the mice were euthanized, and the tumor masses were weighed and then collected together with major organs for hematoxylin and eosin (H&E) staining.

2.11 Histological examination

The collected tumors and major organs were fixed in 10% formalin, embedded in paraffin, sectioned, and stained with H&E. The histological slices were imaged under an inverted optical microscope.

2.12 Blood analysis

Six ICR mice were randomly subdivided into two groups. Mice in the experimental group were intravenously injected with TPE-red-PEG-RGD nanoparticles (10 mg·kg^{-1}), while the mice in the control group were all injected with 200 μL of PBS (1×); 24 h later, venous blood samples were collected into evacuated tubes containing EDTA and sodium citrate (anticoagulants) and non-anticoagulant agents. The blood analysis was carried out on a Coulter LH 780 Analyzer (Beckman) and Architect C16000 (Abbott).

2.13 Statistics

All the results presented are mean ± SD. Statistical analysis was performed by Student's t test (*P < 0.05, **P < 0.01, and ***P < 0.001).

3 Results and discussion

3.1 Synthesis and characterization of TPE-red-PEG-RGD nanoparticles

We synthesized TPE-red according to our previous report [52]. The entire procedure for fabrication of our nanoparticles is illustrated in Scheme 1(a). First, we encapsulated TPE-red with a biocompatible amphiphilic polymer: DSPE-PEG$_{2000}$-Mal [62, 63], abbreviated as TPE-red-PEG. The long PEG chains were intended to reduce the phagocytosis of nanoparticles by the reticuloendothelial system [64, 65]. We then modified the target moiety c(RGDfc) through click chemistry between –SH and maleimide at the surface of TPE-red-PEG, thus obtaining TPE-red-PEG-RGD nanoparticles. The conjugation efficiency of c(RGDfc) using Ellman's reagent was calculated and found to be 85% [56], and the drug-loading ratio of TPE-red was found to be 4.67%. The morphology and cross-sectional structure of TPE-red-PEG-RGD nanoparticles were first checked by TEM (Fig. 1(a)). The average size of the nanoparticles was ~ 50 nm, which was confirmed by dynamic light scattering (DLS) analysis (inset in Fig. 1(a)). The absorption spectra of TPE-red in a THF solution and TPE-red-PEG-RGD nanoparticles in PBS are shown in Fig. 1(b). We found that, compared with the absorption spectrum of TPE-red, the spectrum of TPE-red-PEG-RGD nanoparticles kept the same shape but had a slight red-shift in wavelength because of the encapsulation process. The fluorescence spectra were recorded using a lab-built fluorescence detection system (Fig. S1 in the ESM). We adjusted the absorption of both TPE-red and TPE-red-PEG-RGD nanoparticles to the same value and acquired the spectra under the same conditions. As shown in Fig. 1(c), at the same location of the peak at 650 nm, the fluorescence of TPE-red-PEG-RGD nanoparticles is much stronger than that of TPE-red, thus confirming the AIE nature of the materials. Meanwhile, we also compared the fluorescence-emitting ability of TPE-red-PEG-RGD nanoparticles and nanoparticles of a common PS, chlorin e6. Figure S2 in the ESM shows that at the same concentration of 100 μg·mL^{-1}, the fluorescence of TPE-red-PEG-RGD nanoparticles was obviously stronger than that of chlorin e6 nanoparticles, indicating the advantage of TPE-red-PEG-RGD nanoparticles over traditional PSs. We then verified the ability of TPE-red-PEG-RGD nanoparticles to produce ROS by means of a common ROS probe, ABDA [66]. During irradiation with 450 nm continuous wave laser light, when mixed with TPE-red-PEG-RGD nanoparticles, the absorption of ABDA at 377 nm kept decreasing for 40 min and dropped to ~ 70% of the original value (Fig. 1(d) and Fig. S3(c) in the ESM). At the same time, almost no change could be observed in control groups (Fig. 1(d), and Figs. S3(a) and S3(b) in the ESM). This

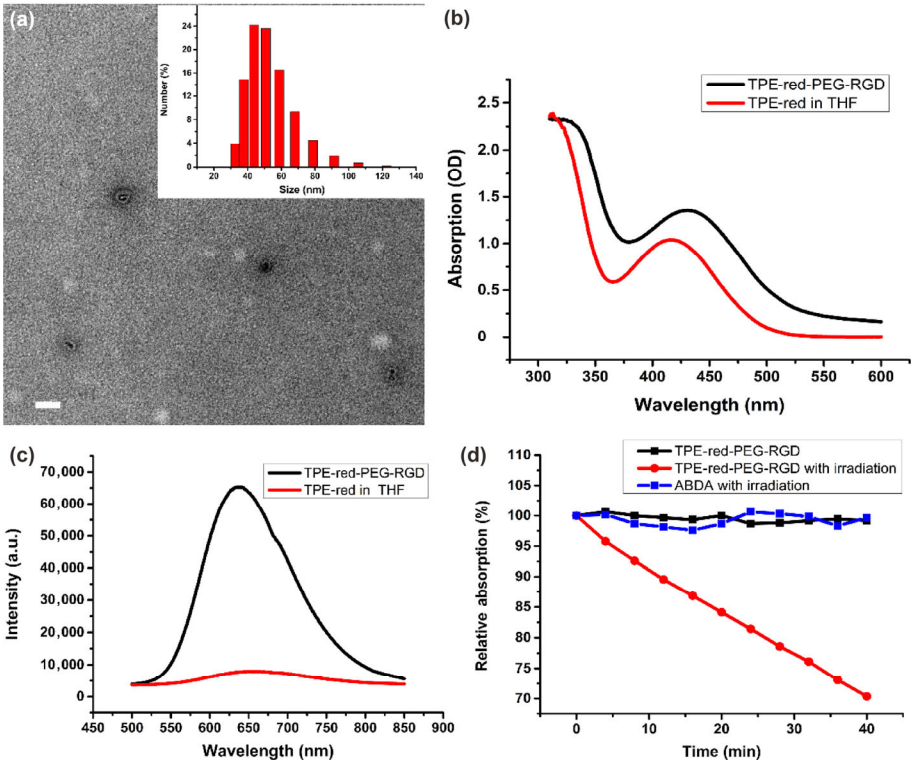

Figure 1 Characteristics of TPE-red-PEG-RGD nanoparticles. (a) TEM image of TPE-red-PEG-RGD nanoparticles (inset: DLS data); (b) absorption spectra and (c) fluorescence spectra of TPE-red-PEG-RGD nanoparticles in PBS (1×) and TPE-red in THF; (d) normalized absorption of ABDA at 377 nm after different treatments.

phenomenon indicated that although the reducibility of c(RGDfc) may have some negative effect, TPE-red-PEG-RGD nanoparticles still have a strong ability to produce ROS continuously during irradiation.

3.2 *In vitro* cell imaging

The targeting and endocytosis abilities of TPE-red-PEG-RGD nanoparticles were verified by two-photon-excited fluorescence cell imaging. We first studied the two-photon-excited fluorescence properties of TPE-red-PEG-RGD nanoparticles; the spectra were recorded on our lab-built system (see the "Experimental" section, Fig. S1 in the ESM, and Fig. 2(a)), and power dependence fitting confirmed the nonlinear optical process (Fig. 2(b)). By comparison methods, we calculated the QY of TPE-red-PEG-RGD nanoparticles: 8.27%. When we substituted this value into the formula of TPACS, we obtained the TPACS of TPE-red-PEG-RGD nanoparticles, 98.085 GM, which is the average value for each dye molecule. If the nanoparticles are regarded as big molecules, then the TPACS amounts to 5.36×10^3 GM for each particle. We employed a scanning microscope for two-photon-excited fluorescence imaging. The signal was excited by a 1,040 fs laser (from an amplified output of a large-mode-area ytterbium-doped PCF oscillator (1,040 nm, 150 fs, 50 MHz)) [57] and collected by an objective lens. Figures 2(c) and 2(d) show the images of UMUC3 cells (human bladder cancer cell line) as seen through a 20× objective lens without and with TPE-red-PEG-RGD nanoparticles (0.2 $\mu g \cdot mL^{-1}$), respectively. Almost all the cells were labeled. We also performed cell imaging through a 60× objective lens to verify the label details and could clearly see that the signal points were distributed well in cells (Fig. 2(e)). By staining cell nuclei with Hoechst 33258, we then found that TPE-red-PEG-RGD nanoaggregates were distributed well around the nucleus (Fig. S5 in the ESM). Furthermore, we compared the endocytosis ability of TPE-red-PEG-RGD nanoparticles using a 20× objective lens on different cell lines (Fig. S6 in the ESM), and these assays revealed an outstanding ability of TPE-red-PEG-RGD nanoparticles to label different cancer cells.

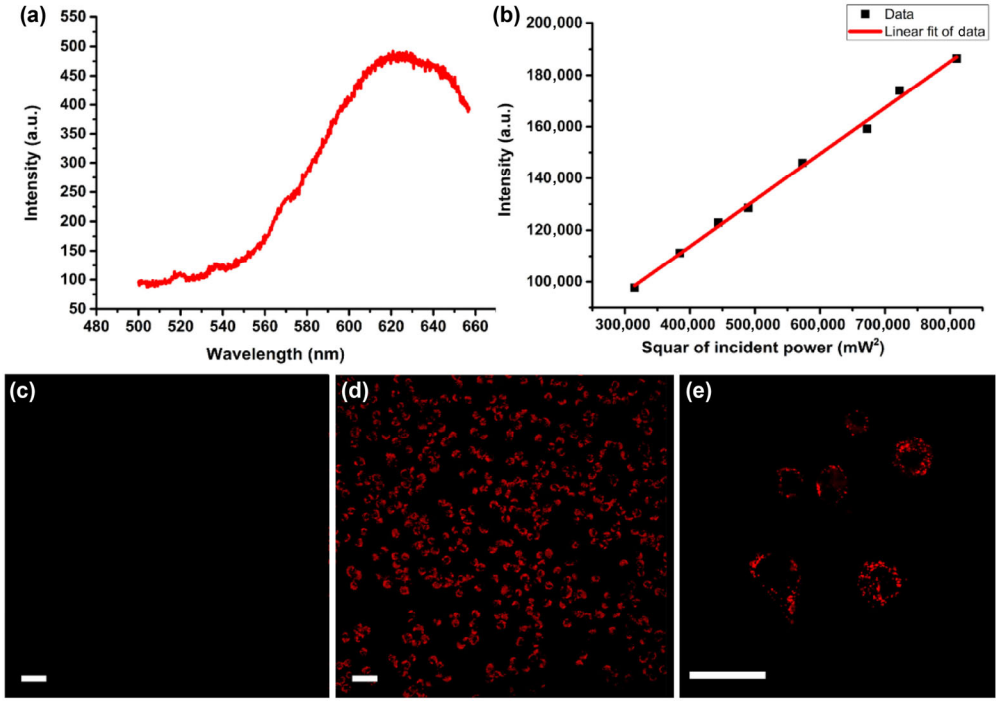

Figure 2 Two-photon excitation properties and *in vitro* cell imaging of UMUC3 cells incubated with TPE-red-PEG-RGD nanoparticles. (a) A two-photon-excited fluorescence spectrum of TPE-red-PEG-RGD nanoparticles; (b) the power dependence and linear fitting of the data; two-photon-excited fluorescence images of UMUC3 cells (c) without nanoparticle treatment as seen through a 20× objective lens and (d), (e) treated with TPE-red-PEG-RGD nanoparticles (0.2 μg·mL^{-1}), as seen through a 20× objective lens and a 60× objective lens, respectively. Scale bar, 50 μm.

3.3 MTT assay

A MTT assay was conducted to study the cytotoxicity in the dark and the PDT efficacy of TPE-red-PEG-RGD nanoparticles [67]. As shown in Fig. 3(a), TPE-red-PEG-RGD nanoparticles were found to have low toxicity in the dark, and the relative cell viability stayed above 90% even at a nanoparticle concentration of 50 μg·mL^{-1}. Upon irradiation with 450 nm laser at irradiance of 200 mW·cm^{-2}, UMUC3 cells without TPE-red-PEG-RGD nanoparticles showed no obvious differences from the control group, whereas the viability of cells incubated with the TPE-red-PEG-RGD nanoparticles decreased obviously as concentration increased. These phenomena indicate that TPE-red-PEG-RGD nanoparticles are minimally toxic in the dark and much more toxic under 450 nm light. Among the cells treated with the same concentration of TPE-red-PEG-RGD nanoparticles (20 μg·mL^{-1}), the viability decreased as the irradiation time increased, further confirming the PDT effect.

3.4 *In vivo* fluorescence imaging

To explore the *in vivo* tumor targeting and labeling capability of TPE-red-PEG-ROS, we analyzed tumor-bearing mice as a tumor xenograft model. The UMUC3 cell line was chosen because of its high malignancy and representativeness [68, 69]. TPE-red-PEG-RGD nanoparticles in PBS (1×) were intravenously injected, and *in vivo* images were captured at 24, 48, and 72 h post-injection. We chose a mouse with a strip-shaped tumor to make the label more distinguishable, and a bright-field photograph is shown in Fig. 4(a). Fluorescent images at 24 h (Fig. 4(b)), 48 h (Fig. 4(c)), and 72 h (Fig. 4(d)) together with the bright-field image suggest that TPE-red-PEG-RGD nanoparticles can label tumor tissues well and last for at least 72 h (Fig. 4(f)). The signal from the tumor site was obviously stronger than that from peripheral tissue except for the reticuloendothelial system (e.g., liver and spleen) and lymph, and the shape of the labeled area coincided well with that of the tumor. Spectra acquired from

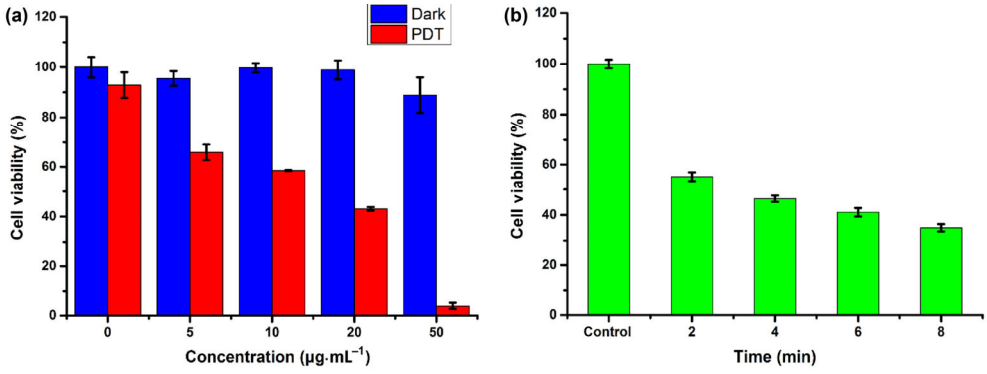

Figure 3 (a) Viability data on UMUC3 cells treated with different concentrations of TPE-red-PEG-RGD nanoparticles in the dark and after PDT (450 nm, 40 mW, 6 min). (b) Viability of UMUC3 cells irradiated for different periods after treatment with the same concentration of TPE-red-PEG-RGD nanoparticles (20 μg·mL^{-1}). Error bars indicate SD.

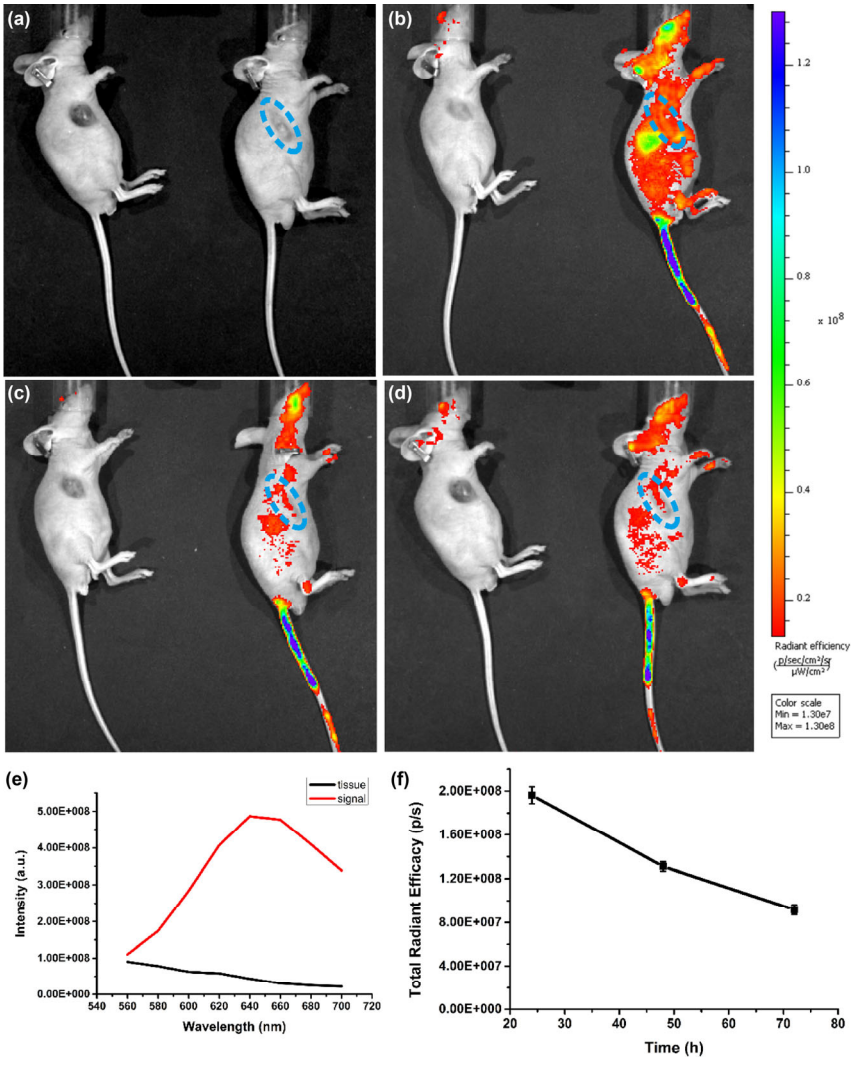

Figure 4 *In vivo* imaging experiments on tumor-bearing mice treated with TPE-red-PEG-RGD nanoparticles. (a) A photograph of mice in the control group (left) and experimental group (right); (b)–(d) fluorescent images of mice 24, 48, and 72 h post-injection in the control group (left) and experimental group (right); (e) spectra of TPE-red-PEG-RGD nanoparticles (taken from the injection port in the tail) and tissue autofluorescence (taken from the back of a mouse in the control group); (f) changing tendency of total radiant efficacy in the tumor area (circled in blue). Error bars indicate SD.

the injection port in the tail in the experimental group and on the back of a mouse in the control group confirmed that the fluorescence signal is strongly distinguishable from tissue autofluorescence (Fig. 4(e)). With knowledge about organ distributions and metabolic processing of nanoparticles, we can easily recognize the liver, spleen, and lymph, and the additional labeled areas can be identified as tumor tissue. These data will guide us to the exact region to apply PDT.

3.5 *Ex vivo* fluorescence imaging

To make the tissue distribution clearer, *ex vivo* microscopy of a tumor and major organs was carried out. As shown in Figs. S7(a)–S7(c) in the ESM, the tumor was well labeled and only negligible signals could be observed in the heart, lungs, or spleen. As shown in Fig. S7(d) in the ESM, by the fluorescence quantitative analysis of a tumor and major organs, we found that the accumulation of TPE-red-PEG-RGD nanoparticles in a tumor reached a maximum value 48 h post-injection and dropped slightly at 72 h. This result is a little different from that of *in vivo* fluorescence analysis possibly because of the influence of the skin and the blood vessels distributed around tumor tissue. Because the *ex vivo* fluorescence was less affected, we think it can better reflect the accumulation of TPE-red-PEG-RGD nanoparticles in tumor tissue. At the same time, we could detect the sustained accumulation of TPE-red-PEG-RGD nanoparticles in the liver, while the accumulation in kidneys rose and dropped sharply as time went on, possibly indicating the metabolism of TPE-red-PEG-RGD nanoparticles.

3.6 *In vivo* PDT

To further assess the *in vivo* antitumor efficacy of TPE-red-PEG-RGD nanoparticles, 16 tumor-bearing mice were randomly distributed into four groups and subjected to different treatments: (1) PBS, without irradiation; (2) PBS, with irradiation; (3) TPE-red-PEG-RGD nanoparticles (10 mg·kg^{-1}), without irradiation; or (4) TPE-red-PEG-RGD nanoparticles (10 mg·kg^{-1}), with irradiation. The observation lasted for 14 days. After that, the mice were euthanized, and photographs were taken of them and the tumors, shown in Figs. 5(c)

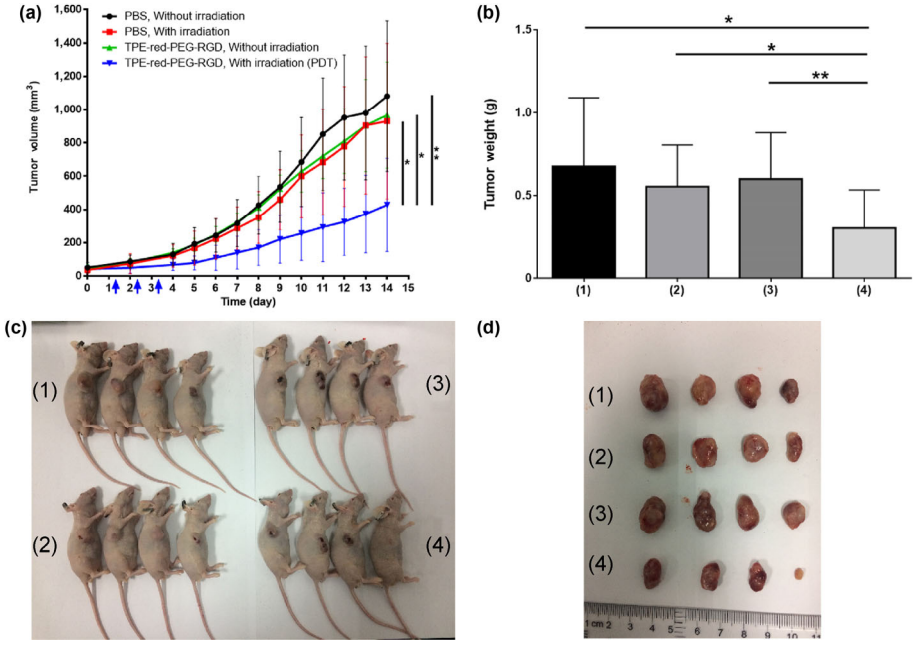

Figure 5 *In vivo* analysis of antitumor effects of TPE-red-PEG-RGD nanoparticles. (a) Change in average tumor volume after different treatments as a function of time (blue arrows indicate the presence of light); (b) average tumor weights 14 days after different treatments; photographs of (c) euthanized mice and (d) tumors. The numbers written on the paper indicate different groups: (1) PBS, no irradiation; (2) PBS, irradiation; (3) TPE-red-PEG-RGD nanoparticles, no irradiation; and (4) TPE-red-PEG-RGD nanoparticles, irradiation (PDT). Error bars indicate SD. Scale bar, 50 μm. (*P < 0.05, **P < 0.01.)

and 5(d), respectively. We recorded the change of tumor volumes. It was found that only when both TPE-red-PEG-RGD nanoparticles and 450 nm laser light were present, could the growth of the tumor volume be noticeably inhibited ($P < 0.001$; Fig. 5(a)), and the tumor growth inhibition rate was found to be as high as 60.4%. In Fig. 5(b), we can see that the final average tumor weight of the PDT group was significantly lower than that in the three control groups ($P < 0.05$). The therapeutic efficacy was confirmed by the examination of tumor tissue sections. Only tumors that were treated with both TPE-red-PEG-RGD nanoparticles and 450 nm irradiation had obvious signs of cell death, while nothing of significance happened to tumors in other groups (Fig. 6).

3.7 *In vivo* toxicity

To evaluate the *in vivo* toxicity of TPE-red-PEG-RGD nanoparticles, the weight of the mice was recorded during the treatment. As shown in Fig. S8 in the ESM, all mice grew healthily, and not much difference was observed. We also checked the slices of major organs in different treatment groups; no obvious inflammation or abnormalities could be found, indicating negligible *in vivo* toxicity of TPE-red-PEG-RGD nanoparticles (Fig. 7).

Besides, biocompatibility of TPE-red-PEG-RGD nanoparticles was evaluated by monitoring standard hematological and biochemical markers. The blood chemistry as the indicator of toxicity in mice treated with TPE-red-PEG-RGD nanoparticles was determined 24 h after intravenous injection of TPE-red-PEG-RGD nanoparticles (10 mg·kg^{-1}). As shown in Figs. S9(a)–S9(f)

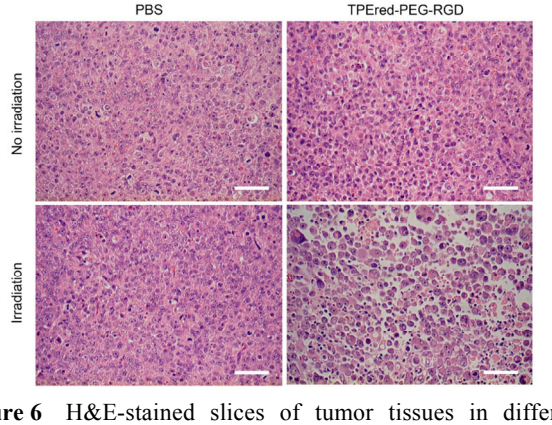

Figure 6 H&E-stained slices of tumor tissues in different treatment groups. Scale bar, 50 μm.

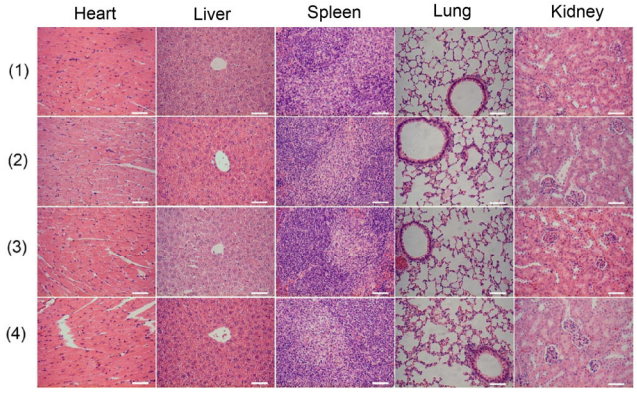

Figure 7 H&E-stained sections of major organs (the heart, liver, spleen, lung, and kidney) of mice after different treatments. The numbers written on the paper indicate different groups: (1) PBS, no irradiation; (2) PBS, irradiation; (3) TPE-red-PEG-RGD nanoparticles, no irradiation; (4) TPE-red-PEG-RGD nanoparticles, irradiation (PDT). Scale bar, 50 μm.

in the ESM, the counts of red blood cells, white blood cells, and platelets revealed no obvious toxicity, as was the case for the mean erythrocyte volume, red blood cell distribution width, and mean platelet volume. Indicators of liver function, including the enzymatic activities of alanine transaminase, aspartate transaminase, alkaline phosphatase, and glutamyl transpeptidase were measured at the same time. As shown in Figs. S9(g)–S9(j) in the ESM, the levels were within the reference range observed in control mice or found in the literature. Markers of kidney function—creatinine, urea, and uric acid—were also quantified, and no signs of kidney impairment were noted (Figs. S9(k)–S9(m) in the ESM).

4 Conclusions

In summary, we demonstrated that dual-function TPE-red-PEG-RGD nanoparticles can be applied to targeted and imaging-guided *in vivo* PDT. Our work has the following advantages: 1) TPE-red-PEG-RGD nanoparticles exploit the AIE nature of TPE-red molecules and enhance the fluorescence signals instead of undergoing aggregation-caused quenching like many commonly used PSs; 2) both passive and active targeting were implemented to guarantee therapeutic efficacy, and targeted imaging of tumor regions and high antitumor efficacy could be achieved at a reasonably low dose, which may cause fewer adverse

effects; 3) the structure of TPE-red-PEG-RGD nanoparticles is simple and they are easy to fabricate, which may facilitate further research and mass production. Our results show a promising role of AIE nanoparticles in imaging-guided *in vivo* PDT, both in biomedical research and clinical applications.

Acknowledgements

This work was supported by the National Basic Research Program of China (973 Program) (Nos. 2013CB834704 and 2011CB503700), the National Natural Science Foundation of China (NSFC) (No. 11621101), and the Science and Technology Department of Zhejiang Province (No. 2010R50007)

Electronic Supplementary Material: Supplementary material (supplementary figures; schematic illustration of the lab-built fluorescence detect system; photograph of aqueous dispersion of TPE-red-PEG-RGD and Chlorin e6 nanoparticles under daylight and under UV lamp; absorption spectra of ABDA containing solutions with different treatments; schematic illustration of the two-photon excited fluorescence imaging system; fluorescence images of UMUC3 cells after incubating them with TPE-red-PEG-RGD and stained with heochst 33258; *ex vivo* imaging studies of tumor bearing mice treated with TPE-red-PEG-RGD; average body weight variation of the mice during the treatment; blood analysis results for mice 24 h post injection of TPE-red-PEG-RGD and mice in control group) is available in the online version of this article at https://doi.org/10.1007/s12274-017-1906-7.

References

[1] Siegel, R. L.; Miller, K. D.; Jemal, A. Cancer statistics, 2015. *CA-Cancer J. Clin.* **2015**, *65*, 5–29.

[2] Siegel, R. L.; Miller, K. D.; Jemal, A. Cancer statistics, 2016. *CA-Cancer J. Clin.* **2016**, *66*, 7–30.

[3] Chen, W. Q.; Zheng, R. S.; Baade, P. D.; Zhang, S. W.; Zeng, H. M.; Bray, F.; Jemal, A.; Yu, X. Q.; He, J. Cancer statistics in China, 2015. *CA-Cancer J. Clin.* **2016**, *66*, 115–132.

[4] Miller, K. D.; Siegel, R. L.; Lin, C. C.; Mariotto, A. B.; Kramer, J. L.; Rowland, J. H.; Stein, K. D.; Alteri, R.; Jemal, A. Cancer treatment and survivorship statistics, 2016. *CA-Cancer J. Clin.* **2016**, *66*, 271–289.

[5] Siegel, R. L.; Miller, K. D.; Jemal, A. Cancer statistics, 2017. *CA-Cancer J. Clin.* **2017**, *67*, 7–30.

[6 Early Breast Cancer Trialists' Collaborative Group (EBCTCG). Effects of radiotherapy and of differences in the extent of surgery for early breast cancer on local recurrence and 15-year survival: An overview of the randomised trials. *Lancet* **2005**, *366*, 2087–2106.

[7] Cunningham, D.; Allum, W. H.; Stenning, S. P.; Thompson, J. N.; van de Velde, C. J. H.; Nicolson, M.; Scarffe, J. H.; Lofts, F. J.; Falk, S. J.; Iveson, T. J. et al. Perioperative chemotherapy versus surgery alone for resectable gastroesophageal cancer. *N. Engl. J. Med.* **2006**, *355*, 11–20.

[8] De Angelis, R.; Bugatti, L.; Cerioni, A.; Del Medico, P.; Filosa, G. Diffuse scleroderma occurring after the use of paclitaxel for ovarian cancer. *Clin. Rheumatol.* **2003**, *22*, 49–52.

[9] Griffin, A. M.; Butow, P. N.; Coates, A. S.; Childs, A. M.; Ellis, P. M.; Dunn, S. M.; Tattersall, M. H. On the receiving end. V: Patient perceptions of the side effects of cancer chemotherapy in 1993. *Ann. Oncol.* **1996**, *7*, 189–195.

[10] Allison, R. R.; Sibata, C.; Patel, R. Future radiation therapy: Photons, protons and particles. *Future Oncol.* **2013**, *9*, 493–504.

[11] Gleave, M. E.; Monia, B. P. Antisense therapy for cancer. *Nat. Rev. Cancer* **2005**, *5*, 468–479.

[12] Peer, D.; Karp, J. M.; Hong, S.; FaroKHzad, O. C.; Margalit, R.; Langer, R. Nanocarriers as an emerging platform for cancer therapy. *Nat. Nanotechnol.* **2007**, *2*, 751–760.

[13] Davis, M. E.; Chen, Z.; Shin, D. M. Nanoparticle therapeutics: An emerging treatment modality for cancer. *Nat. Rev. Drug Discov.* **2008**, *7*, 771–782.

[14] Grivennikov, S. I.; Greten, F. R.; Karin, M. Immunity, inflammation, and cancer. *Cell* **2010**, *140*, 883–899.

[15] Semenza, G. L. Targeting HIF-1 for cancer therapy. *Nat. Rev. Cancer* **2003**, *3*, 721–732.

[16] Kelkar, S. S.; Reineke, T. M. Theranostics: Combining imaging and therapy. *Bioconjugate Chem.* **2011**, *22*, 1879–1903.

[17] Gao, X. H.; Yue, Q.; Liu, Z. N.; Ke, M. J.; Zhou, X. Y.; Li, S. H.; Zhang, J. P.; Zhang, R.; Chen, L.; Mao, Y. et al. Guiding brain-tumor surgery via blood–brain-barrier-permeable gold nanoprobes with acid-triggered MRI/SERRS signals. *Adv. Mater.* **2017**, *29*, 1603917.

[18] Wang, C.; Cheng, L.; Liu, Y. M.; Wang, X. J.; Ma, X. X.; Deng, Z. Y.; Li, Y. G.; Liu, Z. Imaging-guided pH-sensitive photodynamic therapy using charge reversible upconversion nanoparticles under near-infrared light. *Adv. Funct. Mater.* **2013**, *23*, 3077–3086.

[19] Lv, R. C.; Yang, P. P.; He, F.; Gai, S. L.; Yang, G. X.; Dai, Y. L.; Hou, Z. Y.; Lin, J. An imaging-guided platform for synergistic photodynamic/photothermal/chemo-therapy with pH/temperature-responsive drug release. *Biomaterials* **2015**, *63*, 115–127.

[20] Huang, P.; Lin, J.; Wang, S. J.; Zhou, Z. J.; Li, Z. M.; Wang, Z.; Zhang, C. L.; Yue, X. Y.; Niu, G.; Yang, M. et al. Photosensitizer-conjugated silica-coated gold nanoclusters for fluorescence imaging-guided photodynamic therapy. *Biomaterials* **2013**, *34*, 4643–4654.

[21] Dougherty, T. J.; Gomer, C. J.; Henderson, B. W.; Jori, G.; Kessel, D.; Korbelik, M.; Moan, J.; Peng, Q. Photodynamic therapy. *J. Natl. Cancer Inst.* **1998**, *90*, 889–905.

[22] Macdonald, I. J.; Dougherty, T. J. Basic principles of photodynamic therapy. *J. Porphyrins Phthalocyanines* **2001**, *5*, 105–129.

[23] Henderson, B. W.; Dougherty, T. J. How does photodynamic therapy work? *Photochem. Photobiol.* **1992**, *55*, 145–157.

[24] Ormond, A. B.; Freeman, H. Dye sensitizers for photodynamic therapy. *Materials* **2013**, *6*, 817–840.

[25] Lucky, S. S.; Soo, K. C.; Zhang, Y. Nanoparticles in photodynamic therapy. *Chem. Rev.* **2015**, *115*, 1990–2042.

[26] Lao, Y. H.; Phua, K. K. L.; Leong, K. W. Aptamer nanomedicine for cancer therapeutics: Barriers and potential for translation. *ACS Nano* **2015**, *9*, 2235–2254.

[27] Doane, T. L.; Burda, C. The unique role of nanoparticles in nanomedicine: Imaging, drug delivery and therapy. *Chem. Soc. Rev.* **2012**, *41*, 2885–2911.

[28] Yang, G. B.; Gong, H.; Qian, X. X.; Tan, P. L.; Li, Z. W.; Liu, T.; Liu, J. J.; Li, Y. Y.; Liu, Z. Mesoporous silica nanorods intrinsically doped with photosensitizers as a multifunctional drug carrier for combination therapy of cancer. *Nano Res.* **2015**, *8*, 751–764.

[29] Hamidi, M.; Azadi, A.; Rafiei, P. Hydrogel nanoparticles in drug delivery. *Adv. Drug Deliv. Rev.* **2008**, *60*, 1638–1649.

[30] Brannon-Peppas, L.; Blanchette, J. O. Nanoparticle and targeted systems for cancer therapy. *Adv. Drug Deliv. Rev.* **2012**, *64*, 206–212.

[31] Gunnoo, S. B.; Madder, A. Bioconjugation-using selective chemistry to enhance the properties of proteins and peptides as therapeutics and carriers. *Org. Biomol. Chem.* **2016**, *14*, 8002–8013.

[32] Bao, C. C.; Conde, J.; Pan, F.; Li, C.; Zhang, C. L.; Tian, F. R.; Liang, S. J.; de la Fuente, J. M.; Cui, D. X. Gold nanoprisms as a hybrid *in vivo* cancer theranostic platform for *in situ* photoacoustic imaging, angiography, and localized hyperthermia. *Nano Res.* **2016**, *9*, 1043–1056.

[33] Valente, G.; Depalo, N.; de Paola, I.; Iacobazzi, R. M.; Denora, N.; Laquintana, V.; Comparelli, R.; Altamura, E.; Latronico, T.; Altomare, M. et al. Integrin-targeting with peptide-bioconjugated semiconductor-magnetic nanocrystalline heterostructures. *Nano Res.* **2016**, *9*, 644–662.

[34] Hobbs, S. K.; Monsky, W. L.; Yuan, F.; Roberts, W. G.; Griffith, L.; Torchilin, V. P.; Jain, R. K. Regulation of transport pathways in tumor vessels: Role of tumor type and microenvironment. *Proc. Natl. Acad. Sci. USA* **1998**, *95*, 4607–4612.

[35] Maeda, H.; Wu, J.; Sawa, T.; Matsumura, Y.; Hori, K. Tumor vascular permeability and the EPR effect in macromolecular therapeutics: A review. *J. Control. Release* **2000**, *65*, 271–284.

[36] Birks, J. B. *Photophysics of Aromatic Molecules*; Wiley-Interscience: London, **1970**.

[37] Sekkat, N.; van den Bergh, H.; Nyokong, T.; Lange, N. Like a bolt from the blue: Phthalocyanines in biomedical optics. *Molecules* **2012**, *17*, 98–144.

[38] Ju, E. G.; Dong, K.; Chen, Z. W.; Liu, Z.; Liu, C. Q.; Huang, Y. Y.; Wang, Z. Z.; Pu, F.; Ren, J. S.; Qu, X. G. Copper(II)-graphitic carbon nitride triggered synergy: Improved ROS generation and reduced glutathione levels for enhanced photodynamic therapy. *Angew. Chem., Int. ed.* **2016**, *55*, 11467–11471.

[39] Liu, C. Q.; Chen, Z. W.; Wang, Z. Z.; Li, W.; Ju, E. G.; Yan, Z. Q.; Liu, Z.; Ren, J. S.; Qu, X. G. A graphitic hollow carbon nitride nanosphere as a novel photochemical internalization agent for targeted and stimuli-responsive cancer therapy. *Nanoscale* **2016**, *8*, 12570–12578.

[40] Ding, D.; Li, K.; Liu, B.; Tang, B. Z. Bioprobes based on AIE fluorogens. *Acc. Chem. Res.* **2013**, *46*, 2441–2453.

[41] Luo, J. D.; Xie, Z. L.; Lam, J. W. Y.; Cheng, L.; Chen, H. Y.; Qiu, C. F.; Kwok, H. S.; Zhan, X. W.; Liu, Y. Q.; Zhu, D. B. et al. Aggregation-induced emission of 1-methyl-1,2,3,4,5-pentaphenylsilole. *Chem. Commun.* **2001**, 1740–1741.

[42] Tang, B. Z.; Zhan, X. W.; Yu, G.; Sze Lee, P. P.; Liu, Y. Q.; Zhu, D. B. Efficient blue emission from siloles. *J. Mater. Chem.* **2001**, *11*, 2974–2978.

[43] Mei, J.; Leung, N. L. C.; Kwok, R. T. K.; Lam, J. W. Y.; Tang, B. Z. Aggregation-induced emission: Together we shine, united we soar! *Chem. Rev.* **2015**, *115*, 11718–11940.

[44] Han, K.; Wang, S. B.; Lei, Q.; Zhu, J. Y.; Zhang, X. Z. Ratiometric biosensor for aggregation-induced emission-guided precise photodynamic therapy. *ACS Nano* **2015**, *9*, 10268–10277.

[45] Chang, C. C.; Hsieh, M. C.; Lin, J. C.; Chang, T. C. Selective photodynamic therapy based on aggregation-induced emission enhancement of fluorescent organic nanoparticles. *Biomaterials* **2012**, *33*, 897–906.

[46] Hsieh, M. C.; Chien, C. H.; Chang, C. C.; Chang, T. C. Aggregation induced photodynamic therapy enhancement

based on linear and nonlinear excited FRET of fluorescent organic nanoparticles. *J. Mater. Chem. B* **2013**, *1*, 2350–2357.

[47] Jayaram, D. T.; Ramos-Romero, S.; Shankar, B. H.; Garrido, C.; Rubio, N.; Sanchez-Cid, L.; Gómez, S. B.; Blanco, J.; Ramaiah, D. *In vitro* and *in vivo* demonstration of photodynamic activity and cytoplasm imaging through TPE nanoparticles. *ACS Chem. Biol.* **2016**, *11*, 104–112.

[48] Yuan, Y. Y.; Feng, G. X.; Qin, W.; Tang, B. Z.; Liu, B. Targeted and image-guided photodynamic cancer therapy based on organic nanoparticles with aggregation-induced emission characteristics. *Chem. Commun.* **2014**, *50*, 8757–8760.

[49] Yuan, Y. Y.; Zhang, C. J.; Gao, M.; Zhang, R. Y.; Tang, B. Z.; Liu, B. Specific light-up bioprobe with aggregation-induced emission and activatable photoactivity for the targeted and image-guided photodynamic ablation of cancer cells. *Angew. Chem., Int. Ed.* **2015**, *54*, 1780–1786.

[50] Gu, B. B.; Wu, W. B.; Xu, G. X.; Feng, G. X.; Yin, F.; Chong, P. H. J.; Qu, J. L.; Yong, K. T.; Liu, B. Precise two-photon photodynamic therapy using an efficient photosensitizer with aggregation-induced emission characteristics. *Adv. Mater.* **2017**, *29*, 1701076.

[51] Li, M.; Gao, Y.; Yuan, Y. Y.; Wu, Y. Z.; Song, Z. F.; Tang, B. Z.; Liu, B.; Zheng, Q. C. One-step formulation of targeted aggregation-induced emission dots for image-guided photodynamic therapy of cholangiocarcinoma. *ACS Nano* **2017**, *11*, 3922–3932.

[52] Hu, F.; Huang, Y. Y.; Zhang, G. X.; Zhao, R.; Yang, H.; Zhang, D. Q. Targeted bioimaging and photodynamic therapy of cancer cells with an activatable red fluorescent bioprobe. *Anal. Chem.* **2014**, *86*, 7987–7995.

[53] Xu, S. D.; Yuan, Y. Y.; Cai, X. L.; Zhang, C. J.; Hu, F.; Liang, J.; Zhang, G. X.; Zhang, D. Q.; Liu, B. Tuning the singlet-triplet energy gap: A unique approach to efficient photosensitizers with aggregation-induced emission (AIE) characteristics. *Chem. Sci.* **2015**, *6*, 5824–5830.

[54] Dall'Angelo, S.; Zhang, Q. Z.; Fleming, I. N.; Piras, M.; Schweiger, L. F.; O'Hagan, D.; Zanda, M. Efficient biocon-jugation of 5-fluoro-5-deoxy-ribose (FDR) to RGD peptides for positron emission tomography (PET) imaging of $\alpha_v\beta_3$ integrin receptor. *Org. Biomol. Chem.* **2013**, *11*, 4551–4558.

[55] Wang, D.; Qian, J.; He, S. L.; Park, J. S.; Lee, K. S.; Han, S. H.; Mu, Y. Aggregation-enhanced fluorescence in PEGylated phospholipid nanomicelles for *in vivo* imaging. *Biomaterials* **2011**, *32*, 5880–5888.

[56] Ellman, G. L. Tissue sulfhydryl groups. *Arch. Biochem. Biophys.* **1959**, *82*, 70–77.

[57] Qian, J.; Wang, D.; Cai, F. H.; Zhan, Q. Q.; Wang, Y. L.; He, S. L. Photosensitizer encapsulated organically modified silica nanoparticles for direct two-photon photodynamic therapy and *in vivo* functional imaging. *Biomaterials* **2012**, *33*, 4851–4860.

[58] Makarov, N. S.; Drobizhev, M.; Rebane, A. Two-photon absorption standards in the 550–1,600 nm excitation wavelength range. *Opt. Express* **2008**, *16*, 4029–4047.

[59] Oulianov, D. A.; Tomov, I. V.; Dvornikov, A. S.; Rentzepis, P. M. Observations on the measurement of two-photon absorption cross-section. *Opt. Commun.* **2001**, *191*, 235–243.

[60] Williams, A. T. R.; Winfield, S. A.; Miller, J. N. Relative fluorescence quantum yields using a computer-controlled luminescence spectrometer. *Analyst* **1983**, *108*, 1067–1071.

[61] Liu, Q.; Guo, B. D.; Rao, Z. Y.; Zhang, B. H.; Gong, J. R. Strong two-photon-induced fluorescence from photostable, biocompatible nitrogen-doped graphene quantum dots for cellular and deep-tissue imaging. *Nano Lett.* **2013**, *13*, 2436–2441.

[62] Deng, L.; Zhang, Y. Y.; Ma, L. L.; Jing, X. L.; Ke, X. F.; Lian, J. H.; Zhao, Q.; Yan, B.; Zhang, J. F.; Yao, J. Z. et al. Comparison of anti-EGFR-Fab' conjugated immunoliposomes modified with two different conjugation linkers for siRNA delivery in SMMC-7721 cells. *Int. J. Nanomedicine* **2013**, *8*, 3271–3283.

[63] Liu, X. Y.; Ruan, L. M.; Mao, W. W.; Wang, J. Q.; Shen, Y. Q.; Sui, M. H. Preparation of RGD-modified long circulating liposome loading matrine, and its *in vitro* anti-cancer effects. *Int. J. Med. Sci.* **2010**, *7*, 197–208.

[64] Langer, R. Drug delivery and targeting. *Nature* **1998**, *392*, 5–10.

[65] Owens, D. E.; Peppas, N. A. Opsonization, biodistribution, and pharmacokinetics of polymeric nanoparticles. *Int. J. Pharm.* **2006**, *307*, 93–102.

[66] Planas, O.; Macia, N.; Agut, M.; Nonell, S.; Heyne, B. Distance-dependent plasmon-enhanced singlet oxygen production and emission for bacterial inactivation. *J. Am. Chem. Soc.* **2016**, *138*, 2762–2768.

[67] Abe, R.; Ueo, H.; Akiyoshi, T. Evaluation of MTT assay in agarose for chemosensitivity testing of human cancers: Comparison with MTT assay. *Oncology* **1994**, *51*, 416–425.

[68] Mohammed, S. I.; Dhawan, D.; Abraham, S.; Snyder, P. W.; Waters, D. J.; Craig, B. A.; Lu, M.; Wu, L.; Zheng, R.; Stewart, J. et al. Cyclooxygenase inhibitors in urinary bladder cancer: *In vitro* and *in vivo* effects. *Mol. Cancer Ther.* **2006**, *5*, 329–336.

[69] Huang, C.; Neoh, K. G.; Xu, L. Q.; Kang, E. T.; Chiong, E. Polymeric nanoparticles with encapsulated superparamagnetic iron oxide and conjugated cisplatin for potential bladder cancer therapy. *Biomacromolecules* **2012**, *13*, 2513–2520.